metals

MDPI

Article

Anisotropic Elastic and Thermal Properties of M_2InX (M = Ti, Zr and X = C, N) Phases: A First-Principles Calculation

Bo Li, Yonghua Duan *, Mingjun Peng, Li Shen and Huarong Qi

Faculty of Material Science and Engineering, Kunming University of Science and Technology, Kunming 650093, China; lbwlkq9999@163.com (B.L.); pmj5530594@kmust.edu.cn (M.P.); sl_zy99@sina.com (L.S.); qihuarong@163.com (H.Q.)

* Correspondence: duanyh@kust.edu.cn

Abstract: First-principles calculations were used to estimate the anisotropic elastic and thermal properties of Ti_2lnX (X = C, N) and Zr_2lnX (X = C, N) M_2AX phases. The crystals' elastic properties were computed using the Voigt-Reuss-Hill approximation. Firstly, the material's elastic anisotropy was explored, and its mechanical stability was assessed. According to the findings, Ti_2lnC, Ti_2lnN, Zr_2lnC, and Zr_2lnN are all brittle materials. Secondly, the elasticity of Ti_2lnX (X = C, N) and Zr_2lnX (X = C, N) M_2AX phase are anisotropic, and the elasticity of Ti_2lnX (X = C, N) and Zr_2lnX (X = C, N) systems are different; the order of anisotropy is Ti_2lnN > Ti_2lnC, Zr_2lnN > Zr_2lnC. Finally, the elastic constants and moduli were used to determine the Debye temperature and sound velocity. Ti_2lnC has the maximum Debye temperature and sound velocity, and Zr_2lnN had the lowest Debye temperature and sound velocity. At the same time, Ti_2lnC had the highest thermal conductivity.

Keywords: first-principles calculations; elastic anisotropy; MAX phases; thermal conductivity; CASTEP

check for updates

Citation: Li, B.; Duan, Y.; Peng, M.; Shen, L.; Qi, H. Anisotropic Elastic and Thermal Properties of M_2InX (M = Ti, Zr and X = C, N) Phases: A First-Principles Calculation. *Metals* **2022**, *12*, 1111. https://doi.org/10.3390/met12071111

Academic Editor: Guy Makov

Received: 8 June 2022
Accepted: 24 June 2022
Published: 28 June 2022

1. Introduction

The ternary layered compound MAX phase has the common characteristics of ceramics and metals, and has become a research hotspot in the field of structural ceramics for more than 20 years. High damage tolerance and high fracture toughness are essential characteristics that distinguish it from traditional ceramics [1–6]. This type of material has a similar nano-layered crystal structure (space group $P6_3/mmc$), which is named the "$M_{n+1}AX_n$" phase, referred to as MAX phase, where M is a transition metal element, A is a IIIA or IVA group element, and X is C or N, (n = 1~3) [7–9]. MAX phase compounds can be regarded as the formation of a layer of main group atoms inserted into the binary carbon/nitride lattice. Characterization shows the extraordinary properties of MAX phase materials. They have many excellent properties, such as high damage tolerance, high fracture toughness, low hardness, machinability, thermal shock resistance, high damping, high stiffness, and good electrical and thermal conductivity [10,11], etc. Among them, 211-type MAX phase compounds also have similar properties. This extraordinary performance quickly attracted widespread attention in the field of ceramics.

At present, Z. J. Yang et al. have carried out many theoretical studies on the novel hysteresis behavior of Zr_2InC based on plane-wave pseudopotential (PW-PP) density functional theory (DFT) calculations, and the mechanical and electronic properties of Zr_2InC under pressure were investigated using first principles [12]. A.D. Bortolozo et al. investigated the Ti_2InN phase by X-ray diffraction and magnetic and resistivity measurements, and the results clearly showed that Ti_2InN is the first nitride superconductor belonging to the $M_{n+1}AX_n$ family [13]. Sun et al. investigated the relationship between chemical bonds and the elastic properties of M_2AN (M = Ti, Zr, Hf, V, Nb, Ta, Cr, Mo and W, A = Al, Ga and Ge) by calculation [14]. The study showed that with the increase of valence electron concentration, the bulk modulus of M_2AN increases by a factor of 1.8, and the coupling between the MN layer and the A layer weakens. Despite these studies, theoretical studies

of the M_2lnX phase are not sufficient. Previously, MAX carbides have received the greatest attention, while MAX nitrides have received less. In general, the nitride phase and the carbide phase are very similar. Therefore, first-principles calculations are employed to investigate the structure, elastic anisotropy, and thermodynamic properties of Ti_2lnX (X = C, N) and Zr_2lnX (X = C, N) M_2AX phase ceramics, providing a comprehensive complement to previously unexplored areas.

2. Methods

In this work, M_2InX (M = Ti, Zr and X = C, N) MAX phases were analyzed using the Cambridge Sequential Total Energy Package (CASTEP) [15,16] of Density Functional Theory (DFT) [17]. The interactions between electrons and ionic nuclei were calculated using on-the-fly generation (OTFG), ultrasoft pseudopotentials (USPPs), and the Perdew–Wang generalized-gradient approximation (PW91) [18–21] method in generalized gradient approximation (GGA) was utilized to model exchange correlation potential. In this work, the geometric optimization tolerance was set to 5×10^{-6} eV/atom of total energy difference, the maximum ionic Hellmann–Feynman force was 0.01 eV/atom, the maximum ion displacement was 5×10^{-4}, and the maximum stress was 0.02 GPa; the M_2InX phases plan-wave cutoff energy was set to 450 eV and the k-point in the first irreducible Brillouin zone was selected as $10 \times 10 \times 2$. In this calculation, we conducted relevant tests on $1 \times 1 \times 1$, $1 \times 1 \times 2$, $1 \times 2 \times 2$, and $2 \times 2 \times 2$ supercells, and found that when using $1 \times 1 \times 2$, $1 \times 2 \times 2$, $2 \times 2 \times 2$ supercells, the resulting energy change was about 1 meV/atom. The total number of atoms in $1 \times 1 \times 1$, $1 \times 1 \times 2$, $1 \times 2 \times 2$, and $2 \times 2 \times 2$ supercells were 8, 16, 32, and 64, respectively. Considering the computational cost and time, this study finally decided to use a $1 \times 1 \times 2$ supercell for the calculation.

3. Results and Discussion

3.1. Single-Crystal Structural Properties

Firstly, the most stable hexagonal M_2InX (M = Ti, Zr and X = C, N) MAX phase crystal structure was determined, as shown in Figure 1. Fully relaxing atomic locations and lattice parameters yielded a crystal structure in equilibrium. Table 1 displays the computed lattice parameters *a* and *c*, as well as their volumes and formation enthalpies. The calculated structural parameters of the M_2InX phase are in agreement with other experimental results [12,22]. This demonstrates the dependability and precision of the simulations presented in this study, and provided us with the confidence to continue investigating the characteristics of Ti_2lnX (X = C, N) and Zr_2lnX (X = C, N) ceramics. Ti_2lnX (X = C, N) and Zr_2lnX (X = C, N) crystallize in the $P6_3/mmc$-space group with the Wyckoff positions of 4*f* (1/3, 2/3, $Z_{Zr/Ti}$) for Zr/Ti atoms, 2*d* (1/3, 2/3, 3/4) for In atoms, and 2*a* (0, 0, 0) for N/C atoms, and the unit cell was made up of 8 atoms, including 2X, 4M, and 2ln atoms. The atoms were aligned along the *c*-axis in the order X-ln-M-X, as shown in Figure 1.

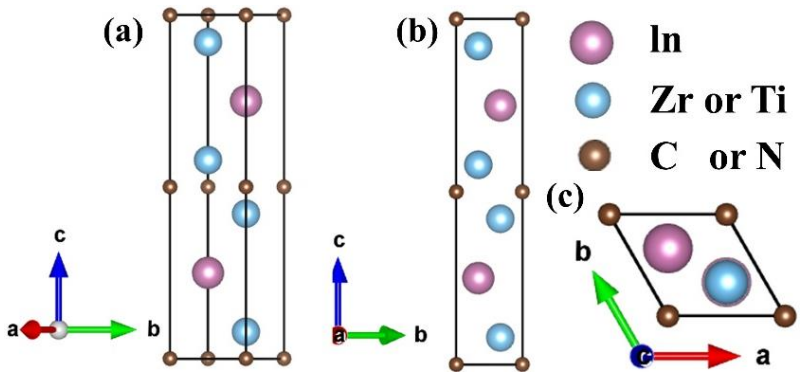

Figure 1. Crystal structure of M_2InX (M = Ti, Zr and X = C, N) MAX phases: (**a**) three-dimensional view, (**b**) side view, (**c**) top view.

Table 1. The lattice parameters, cohesive energy E_c (in eV/atom), and formation enthalpy ΔH_f (in eV/atom) of M_2InX (M = Ti, Zr and X = C, N) MAX phases.

	Lattice Parameters (Å)		V (Å^3)	E_c	ΔH_f	Ref.
	a	c				
Ti_2InC	3.15	14.18	121.67	−7.81	−0.665	This work
	3.14	14.17	120.74		−0.669	Exp. [22]
Ti_2InN	3.10	14.05	116.76	−8.02	−0.667	This work
				−8.01		Exp. [13]
Zr_2InC	3.36	15.04	147.47	−8.30	−0.690	This work
	3.35	15.04	146.62			Theo. [12]
	3.349	14.91	144.8			Theo. [12]
	3.358	15.09	147.437			Theo. [12]
Zr_2AlC					−0.40	Theo. [24]
Zr_2BiC					−4.17	Theo. [24]
Zr_2InN	3.31	14.92	141.25	−8.51	−0.751	This work
				−8.12		Theo. [23]

The computed lattice parameters a and c, their volumes, the formation enthalpy, and cohesive energy are listed in Table 1. As we all know, thermodynamic stability can be understood to some extent as the concept of minimal energy, which states the lower the energy, the greater the system's thermodynamic stability. As a result, thermodynamic stability is described using quantities such as formation enthalpy ΔH_f, and cohesive energy E_c. When the formation enthalpy and cohesive energy are both negative, the structure is stable. Therefore, the greater the negative value, the greater the substance's stability. The calculation is as follows:

$$E_c(M_2InX) = \frac{1}{8}[E(M_2InX) - 4E_{iso}(M) - 2E_{iso}(In) - 2E_{iso}(X)] \quad (1)$$

$$\Delta H_f(M_2InX) = \frac{1}{8}[E(M_2InX) - 4E_{bulk}(M) - 2E_{bulk}(In) - 2E_{bulk}(X)] \quad (2)$$

Here, E is the total energy of M_2InX. E_{bulk}(M), E_{bulk}(In) and E_{bulk}(X) represent the energies of single M, In, and X atoms in a stable state, respectively. E_{iso}(M), E_{iso}(In), and E_{iso}(X) are the energies of isolated M, In, and X atoms, respectively.

Table 1 and Figure 2 show the computed cohesive energy E_c and formation enthalpy ΔH_f of Ti_2InC, Ti_2InN, Zr_2InC, and Zr_2InN, as well as other experimental data for related compounds [12,13,22–24]. The predicted E_c and ΔH_f values for the compounds in Table 1 are negative, indicating that Ti_2InC, Ti_2InN, Zr_2InC, and Zr_2InN are thermodynamically stable and have stronger bond strengths. Furthermore, the sequence of E_c and ΔH_f values is Ti_2InC > Ti_2InN and Zr_2InC > Zr_2InN. Therefore, the order of thermodynamic stability is Ti_2InN > Ti_2InC and Zr_2InN > Zr_2InC. The comprehensive comparison shows that Zr_2InN and Ti_2InN have the highest thermodynamic stability. If Zr_2InN and Ti_2InN continue to be compared, it can be seen that Zr_2InN has the highest thermodynamic stability, which is shown in Figure 2.

3.2. Elastic Properties

This work is based on the stress-strain approach of Hooke's law to analyze mechanical stability, and the elastic constants were determined by applying normal stress, shear stress, and six different deformations. Table 2 shows the calculated elastic constants C_{ij} and elastic compliance constants S_{ij} of Ti_2InC, Ti_2InN, Zr_2InC, and Zr_2InN. Only five elastic constants (C_{11}, C_{12}, C_{13}, C_{33}, C_{44}) are independent for hexagonal crystals [25]. The mechanical stability criteria for hexagonal crystals are given by the following equation [26–28]:

$$C_{11} - C_{12} > 0; C_{44} > 0; C_{11} + C_{12} - 2{C_{13}}^2/C_{33} > 0 \quad (3)$$

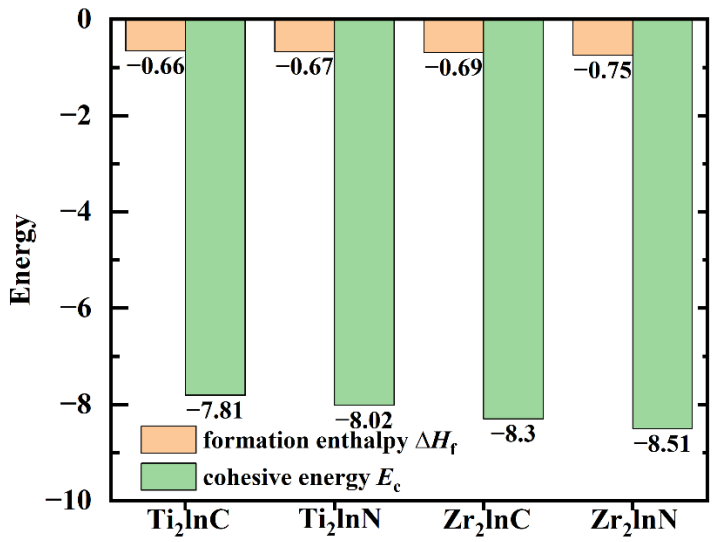

Figure 2. The cohesive energy E_c (in eV/atom) and formation enthalpy ΔH_f (in eV/atom) of M_2InX (M = Ti, Zr and X = C, N) MAX phases.

Table 2. The elastic constants C_{ij} (in GPa) of M_2InX (M = Ti, Zr and X = C, N) MAX phases.

	C_{11}	C_{33}	C_{44}	C_{66}	C_{12}	C_{13}	Ref.
Ti_2lnC	286	244	90	112	64	53	This work
	285	243	83	111	64	52	Theo. [22]
Ti_2lnN	249	228	87	87	54	99	This work
Zr_2lnC	256	241	82	96	64	96	This work
	258	237	83		64	88	Theo. [12]
Zr_2lnN	242	225	89	83	57	88	This work
	237	199	76		55	82	Theo. [23]

Combining the elastic constants calculated in Table 2 and Figure 3, it is not difficult to see that these constants satisfy all the above conditions, proving that Ti_2lnC, Ti_2lnN, Zr_2lnC, and Zr_2lnN are mechanically stable. Usually, the elastic constant represents some important physical meaning, for example, C_{11} and C_{33} correspond to the linear compression resistance of the *a* and *c* axes, respectively. Table 2 reflects that the C_{33} value of M_2lnX is significantly smaller than the C_{11} value, indicating that M_2lnX has a high compressibility along the *c*-axis. To begin with, for the Ti_2lnX (X = C, N) system, Ti_2lnC has the highest C_{11} value (286 GPa) and C_{33} value (244 GPa), while Ti_2lnN has the lowest C_{11} value (229 GPa) and C_{33} value (228 GPa), suggesting that Ti_2lnC is the least compressible along the *a*-axes and *c*-axes, while Ti_2lnN is the most compressible along the *a*-axes and *c*-axes. This is consistent with Ti_2lnC having the strongest chemical bond and Ti_2lnN having the weakest chemical bond [13,22]. It can also be seen that for the system of Zr_2lnX (X = C, N), Zr_2lnC is the most incompressible along the *a*- and *c*-axes, while Zr_2lnN is the most compressible along the *a*- and *c*-axes. From the comparison of the above two systems, it can be understood that Ti_2lnC and Zr_2lnC are the most incompressible of the two systems, respectively. If the values of C_{11} and C_{33} are continuously compared in the M_2lnC (M = Ti, Zr) system, it can be seen that Ti_2lnC > Zr_2lnC, and therefore the compressibility of Ti_2lnC along the *a*-axis and *c*-axis is the smallest, which also confirms that Ti_2lnC has a great elasticity constant.

It is well-known that C_{12}, C_{44}, and C_{66} are related to shear modulus, and larger values of C_{12}, C_{44}, and C_{66} correspond to larger shear modulus. For Ti_2lnX (X = C, N) the order of C_{12}, C_{44}, and C_{66} is Ti_2lnC > Ti_2lnN, while for Zr_2lnX (X = C, N) the order of C_{12}, C_{44}, and C_{66} is Zr_2lnC > Zr_2lnN. Therefore, Ti_2lnC and Zr_2lnC should have the highest shear moduli. Similarly, by comparing the values of C_{12}, C_{44}, and C_{66} in the M_2lnC (M = Ti, Zr) system, it can be seen that Ti_2lnC > Zr_2lnC, which proves that Ti_2lnC has the highest shear modulus.

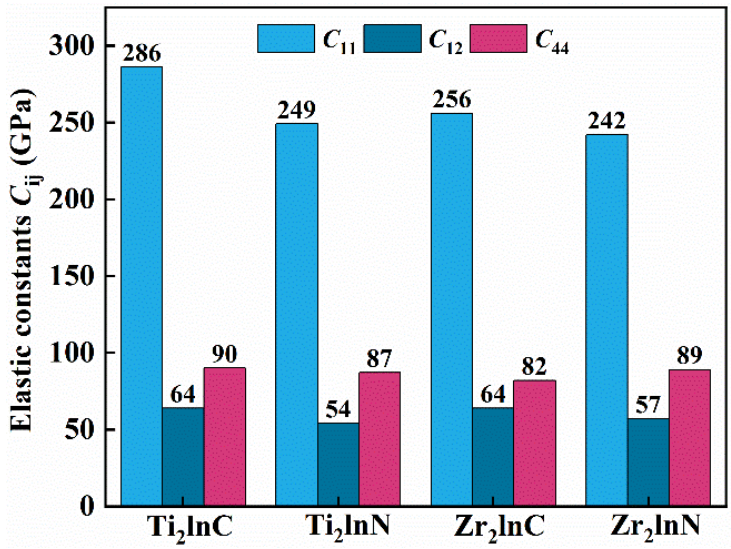

Figure 3. The elastic constants C_{ij} (in Gpa) of M_2InX (M = Ti, Zr and X = C, N) MAX phases.

3.3. Elastic Moduli

In general, using elastic modulus as a parameter to measure the mechanical properties of polycrystals is more convincing than using the elastic constant. In practice, because most materials are polycrystalline, the applied elastic modulus can more accurately describe the anisotropy of the material than the elastic constant. The Reuss-Hill-Voigt approximation is generally used to obtain the elastic modulus for M_2InX phase, which contains Young's modulus E, bulk modulus B, and shear modulus G [24,29,30]. The following are the specific expressions of B_H, E_H, and G_H:

$$G_H = \frac{(G_V + G_R)}{2} \tag{4}$$

$$B_H = \frac{(B_R + B_V)}{2} \tag{5}$$

$$E = \frac{9G_H B_H}{(3B_H + G_H)} \tag{6}$$

Bulk modulus can be specifically divided into lower bulk modulus (B_V) and upper bulk modulus (B_R). Likewise, the shear modulus has a lower shear modulus (G_V) and an upper shear modulus (G_R).

Table 3 shows the estimated and reference data for the elastic modulus M_2InX compound [12,13,23,31]. The results of this computation are obviously close to the findings stated in the reference. Bulk moduli are frequently used to define a material's compressibility under hydrostatic pressure. A higher bulk modulus indicates less compressibility. To put it another way, the higher the bulk modulus, the stiffer the material. It can be seen from Table 3 that for Ti_2InX (X = C, N), the B_H value of Ti_2InC is greater than that of Ti_2InN, indicating that Ti_2InC has higher incompressibility. For Zr_2InX (X = C, N), Zr_2InC has higher incompressibility. It is well-known that the larger bulk modulus in compounds originates from the strong hybridization between orbitals. Therefore, Ti_2InC and Zr_2InC should have the strongest orbital hybridization.

Furthermore, the stiffness of a material can be defined by its Young's modulus; the greater the Young's modulus, the greater the stiffness of the material. Table 3 shows that Ti_2InC and Zr_2InC have the maximum stiffness in the Ti_2InX (X = C, N) and Zr_2InX (X = C, N) systems, respectively. Ti_2InC has the highest stiffness in the M_2InC (M = Ti, Zr) system, because its Young's modulus is greater than that of Zr_2InC. Additionally, the shear modulus can be used to forecast the hardness of a material. In general, the shear modulus characterizes the degree to which the shape of the material is affected by the shear force

acting on it. The larger the shear modulus, the greater the corresponding deformation resistance. Therefore, the greater the shear modulus, the higher the hardness and strength of the material. From the conclusion drawn from the elastic constants in the previous section, it can be seen that Ti_2lnC and Zr_2lnC have the highest shear moduli, so the hardness of both Ti_2lnC and Zr_2lnC is highest. Further comparison of the M_2lnC (M = Ti, Zr) system shows that Ti_2lnC has the largest shear modulus, so the deformation resistance of Ti_2lnC is the largest. Finally, Figure 4a shows the comparison between B, G, and E. Generally, the plastic properties of materials can be characterized by B/G. Judging whether the material is ductile or brittle depends on the value of B/G. If $B/G > 1.75$, the material is plastic; if the contrary, the material is brittle. In addition, it is straightforward to see from the ratios in Table 3 that all four materials are brittle, as these values are all less than the critical value (1.75). In addition, Poisson's ratio (ν) can also be used to measure the brittleness and toughness of materials. When $\nu < 1/3$, it is a brittle material; in addition, the material exhibits toughness. Table 3 shows that the Poisson's ratio of all four materials is less than 0.33. Likewise, Figure 4b can also prove that all four materials are brittle.

Table 3. Calculated bulk modulus B (in GPa), shear modulus G (in Gpa), Poisson's ratio ν, and Young's modulus E (in GPa) of M_2InX (M = Ti, Zr and X = C, N) MAX phases.

	B_V	B_R	B_H	G_V	G_R	G_H	B_H/G_H	E	ν	Ref.
Ti_2lnC										
Ti_2lnN	128.2	127.2	127.7	101.4	100.5	100.9	1.26	239.5	0.187	This work
Zr_2lnC										
Zr_2lnN										
			127					232.04	0.176	Theo. [31]
Ti_2lnN										
Ti_2lnN	123.4	122.7	123.1	78.6	77.8	82.7	1.5	198.1	0.226	This work
Zr_2lnC										
Zr_2lnN										
			121.78							Theo. [13]
Zr_2lnC										
Ti_2lnN	137.4	137.3	137.4	89.5	88.5	89	1.54	216.1	0.217	This work
Zr_2lnC										
Zr_2lnN										
			126.03							Exp. [12]
Zr_2lnN										
Ti_2lnN	134.8	134.8	134.8	82.9	82.2	82.5	1.63	205.7	0.245	This work
Zr_2lnC										
Zr_2lnN										
			134			79		196		Theo. [23]

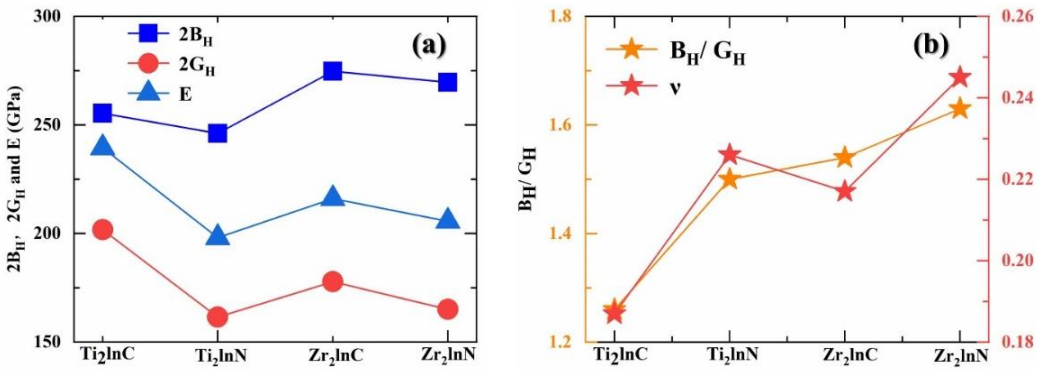

Figure 4. (**a**) Correlations between bulk modulus B (shear modulus G) and Young's modulus (E) of M_2InX (M = Ti, Zr and X = C, N) MAX phases; (**b**) Variations of G_H/B_H and ν of M_2InX (M = Ti, Zr and X = C, N) MAX phases. In graph (**a**), the values of bulk modulus and shear modulus are multiplied by the factor of 2 for a better comparison with Young's modulus.

3.4. Anisotropy in Elastic Moduli

Elastic anisotropy is commonly responsible for the formation and development of microcracks in materials. As a result, the elastic anisotropy of solids must be discussed, and this anisotropy is best defined by three indicators: the anisotropy index A^{U} [32], the percentage of compression anisotropy A_{comp}, and the percentage of shear anisotropy A_{shear} [33–35]. The calculation formula is as follows:

$$A^{\mathrm{U}} = 5\frac{G_V}{G_R} + \frac{B_V}{B_R} - 6 \tag{7}$$

$$A_{\mathrm{comp}} = \frac{B_V - B_R}{B_V + B_R} \times 100\% \tag{8}$$

$$A_{\mathrm{shear}} = \frac{G_V - G_R}{G_V + G_R} \times 100\% \tag{9}$$

$$A_1 = \frac{4C_{44}}{C_{11}+C_{33}-2C_{13}} \tag{10}$$

$$A_2 = \frac{4C_{55}}{C_{22}+C_{33}-2C_{23}} \tag{11}$$

$$A_3 = \frac{4C_{66}}{C_{11}+C_{22}-2C_{12}} \tag{12}$$

Table 4 shows the anisotropy indices of the obtained ceramics of M_2InX phases. Figure 5 depicts the variation of A^{U} with A_{shear}. From Table 4, it can be seen that for Ti_2lnX (X = C, N), the A^{U} value of Ti_2lnC (0.063) is smaller than that of Ti_2lnN (0.042). For Zr_2lnX (X = C, N), the A^{U} value of Zr_2lnC is smaller than that of Zr_2lnN. Because the A^{U} value is proportional to the elastic anisotropy, the order of elastic anisotropy is Ti_2lnN > Ti_2lnC and Zr_2lnN > Zr_2lnC. It shows that Ti_2lnC and Zr_2lnC have better performance and lower possibility of microcracks.

Table 4. Calculated elastic anisotropic indexes (A^{U}, A_{comp}, A_{shear}, A_1, A_2, A_3) of M_2InX (M = Ti, Zr and X = C, N) of MAX phases.

	A^{U}	A_{comp} (%)	A_{shear} (%)	A_1	A_2	A_3
Ti_2lnC Ti_2lnN Zr_2lnC Zr_2lnN	0.053	0.004	0.005	0.851	0.851	1.000
Ti_2lnN Ti_2lnN Zr_2lnC Zr_2lnN	0.059	0.003	0.006	1.622	1.622	1.000
Zr_2lnC Ti_2lnN Zr_2lnC Zr_2lnN	0.034	0.001	0.004	1.072	1.072	1.000
Zr_2lnN Ti_2lnN Zr_2lnC Zr_2lnN	0.043	0.001	0.006	1.225	1.225	1.000

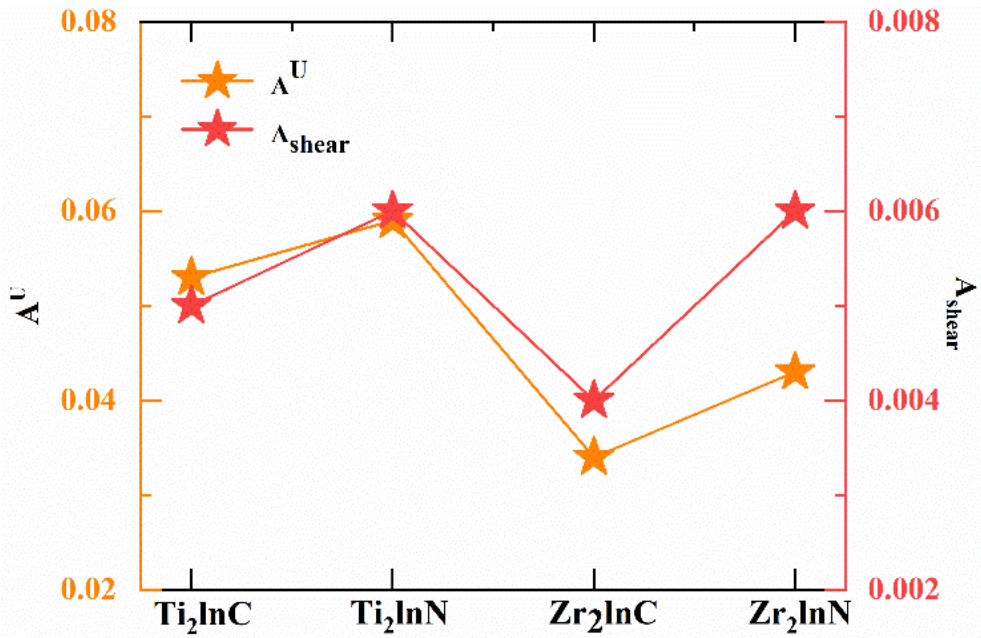

Figure 5. Variations of A^{U} and A_{shear} of M_2InX (M = Ti, Zr and X = C, N) MAX phases.

A_{comp} is used to reflect the compressible anisotropy of the material. From the data in Table 4, it can be seen that the A_{comp} value of Ti_2lnC is the largest (0.004%), indicating that it has the strongest elastic anisotropy. In addition, it can be seen from A_{shear} that Ti_2lnN (0.006) and Zr_2lnN (0.006) have the highest shear elastic anisotropy. Meanwhile, from the A_{shear} value, Ti_2lnC (0.005) and Zr_2lnC (0.004) have the lowest anisotropy of shear modulus. A_1 denotes shear anisotropy in the (100) plane, A_2 shear anisotropy in the (010) plane, and A_3 shear anisotropy in the (001) plane. Table 4 shows the $|A_1 - 1|$ values of Ti_2lnX (X = C, N) and Zr_2lnX (X = C, N). Ti_2lnN and Zr_2lnN have the highest absolute values, respectively, indicating that the shear anisotropy is high. On the other hand, Ti_2lnC and Zr_2lnC have the lowest shear anisotropy on the (100) and (010) planes, respectively. The shear anisotropy results for A_1 agree with those of A_{shear}. Therefore, the order of shear anisotropy is consistent with the order of elastic anisotropy. To sum up, the elastic anisotropy order of the M_2InX system is $Ti_2InX > Zr_2InX$ (X = C, N) and $M_2InN > M_2InC$ (M = Ti, Zr).

Crystal orientation, or the arrangement of crystal atoms in distinct crystal planes and orientations, can also influence elastic anisotropy. As a result, the elastic modulus anisotropy of the M_2InX phase is represented by the 3D surface structure using the following formula [36–38]:

$$\frac{1}{B} = (S_{11}+S_{12}+S_{13})-(S_{11}+S_{12}-S_{13}-S_{33})l_3^2 \tag{13}$$

$$\frac{1}{G} = S_{44} + \left[(S_{11}-S_{12}) - \frac{1}{2}S_{44}\right]\left(1-l_3^2\right)+2(S_{11}+S_{33}-2S_{13}-S_{44})l_3^2(1-l_3^2\Big) \tag{14}$$

$$\frac{1}{E} = S_{11}\left(1-l_3^2\right)^2+S_{33}l_3^4+(2S_{13}+S_{44})l_3^2(1-l_3^2\Big) \tag{15}$$

In this case, l_3 represents the direction cosine.

Figures 6 and 7 display the 3D surface structures of Ti_2lnC, Ti_2lnN, Zr_2lnC, and Zr_2lnN in terms of E, B, and G. Elastic isotropy may be described if the spherical 3D surface structure does not stray significantly from the sphere. Otherwise, it is anisotropic.

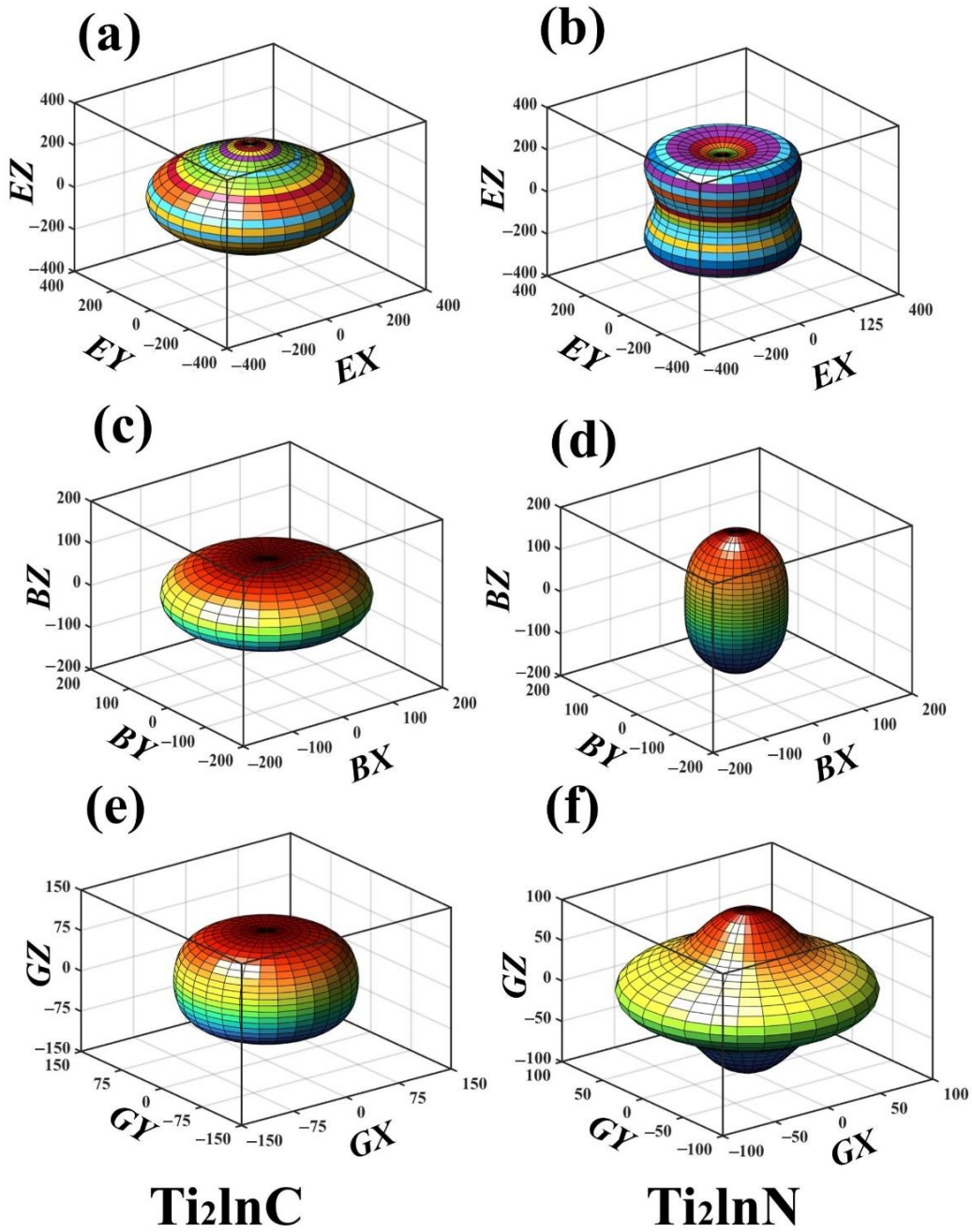

Figure 6. Three-dimensional surface constructions of E (**a**,**b**), B (**c**,**d**) and G (**e**,**f**) of M_2InX (M = Ti, Zr and X = C, N) MAX phases. The unit is GPa.

As can be seen from Figures 6 and 7, for bulk modulus, the 3D views of Ti_2lnC and Zr_2lnC show significant compression along the *c*-axis, while the 3D views of Ti_2lnN and Zr_2lnN show significant compression along the *a*- and *b*-axes. Combined with the data analysis in Table 5, the $B[100]/B[1]$ values of Ti_2lnC, Zr_2lnC, Ti_2lnN, and Zr_2lnN have a large deviation from 1, which can also indicate that the materials are anisotropic.

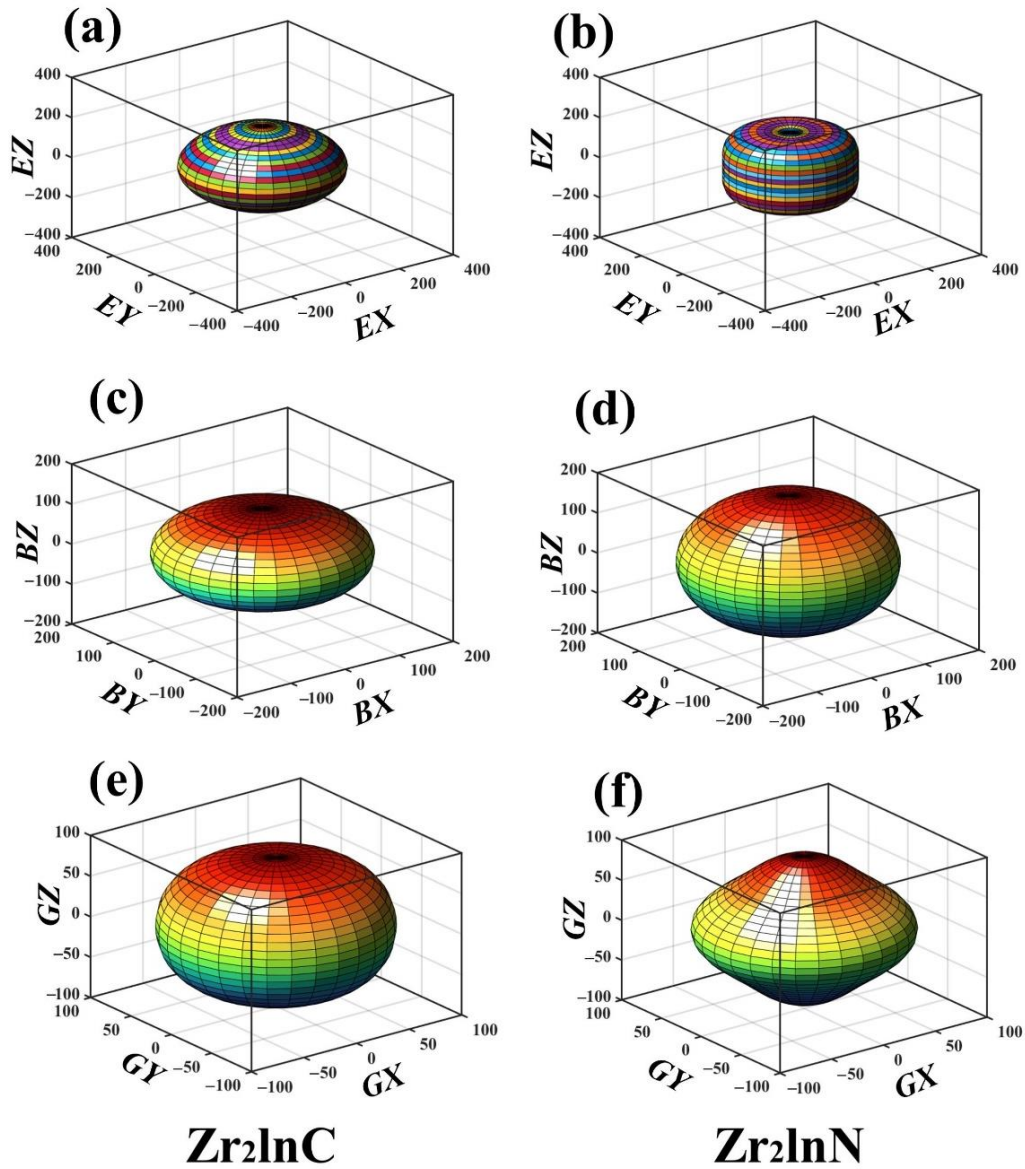

Figure 7. Three-dimensional surface constructions of *E* (**a**,**b**), *B* (**c**,**d**) and *G* (**e**,**f**) of Zr $_2$InX (X = C, N) MAX phases. The unit is GPa.

Table 5. Calculated uniaxial elastic moduli in the [100], [10] and [1] directions (in GPa) of M_2InX (M = Ti, Zr and X = C, N) MAX phases.

		Ti_2InC	Ti_2InN	Zr_2InC	Zr_2InN
E	[1]	304	205	211	174
	[10]	309	216	215	174
	[100]	309	216	215	180
	[100]/[1]	1.02	1.05	1.02	1.04
B	[1]	160	86	156	163
	[10]	172	163	160	170
	[100]	172	163	160	170
	[100]/[1]	1.08	1.90	1.03	1.04
G	[1]	122	118	112	80
	[10]	125	122	115	84
	[100]	125	122	115	84
	[100]/[1]	1.02	1.03	1.03	1.05

When the shear moduli of Ti_2lnN and Zr_2lnN are compared to those of a spherical shape, it is obvious that their shapes are considerably different. As a result, Ti_2lnN and Zr_2lnN shear moduli are anisotropic. Ti_2lnN and Zr_2lnN shear moduli also are anisotropic, and the anisotropy order is Ti_2lnN > Ti_2lnC and Zr_2lnC > Zr_2lnN. Ti_2lnN has a substantially higher degree of shear anisotropy than Zr_2lnN. At the same time, this conclusion is compatible with the previously reported order of percent shear anisotropy. When compared to bulk and shear modulus, Young's modulus E considers both bulk modulus B and shear modulus G. The 3D plots of the Young's modulus of M_2InX (M = Ti, Zr and X = C, N) MAX phases are more compressible along the *a*- and *b*-axes than the *c*-axis, as shown in Figures 6 and 7. Ti_2lnN is more anisotropic than Ti_2lnC, whereas Zr_2lnN is more anisotropic than Zr_2lnN.

The three-dimensional elastic modulus graph shows that Ti_2lnN and Zr_2lnN are elastically anisotropic, with Ti_2lnN having more elastic anisotropy than Zr_2lnN. This is consistent with the A^U value results presented above.

To further illustrate the elastic anisotropy of M_2InX (M = Ti, Zr and X = C, N) MAX phases, Figure 8 plots the 2D projections of the elastic modulus of the M_2InX system on crystal planes (001) and (100), respectively. Based on Figure 8, Table 5 shows the elastic modulus of the M_2InX phases. As can be shown in Table 5, the $G[100]/G[1]$ values of Ti_2lnC and Ti_2lnN are 1.02 and 1.03, respectively, indicating that there is a divergence between $G[100]/G[1]$ and 1, indicating that the material has a greater shear modulus and anisotropy. As a result, Ti_2lnN has the largest shear modulus anisotropy, followed by Ti_2lnC, showing that the order of anisotropy of G is Ti_2lnN > Ti_2lnC. Zr_2lnC and Zr_2lnN have $G[100]/G[1]$ values of 1.03 and 1.05, respectively, showing that the anisotropic order of G is Zr_2lnN > Zr_2lnC. This is consistent with the results of A_1 above.

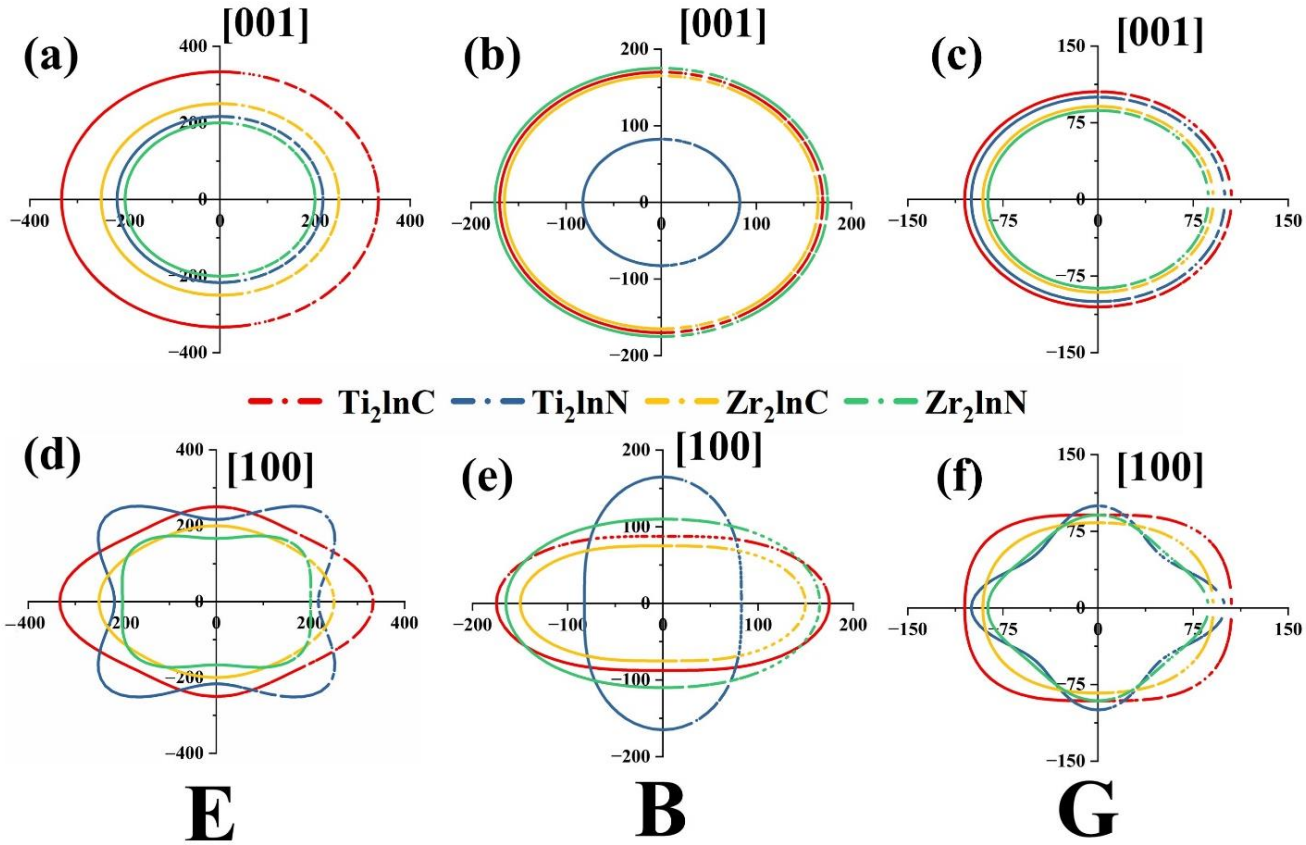

Figure 8. Projections of E (**a**,**b**), B (**c**,**d**) and G (**e**,**f**) of M_2InX (M = Ti, Zr and X = C, N) MAX phases. The unit is GPa.

The $E[100]/E[1]$ values of Ti_2lnC and Ti_2lnN are 1.02 and 1.05, respectively, as shown in Table 5. Zr_2lnC and Zr_2lnN have $E[100]/E[1]$ values of 1.02 and 1.04, respectively. As a result, the anisotropic order of E is $Ti_2lnN > Ti_2lnC$, $Zr_2lnN > Zr_2lnC$. This is consistent with the A^U results.

The expected values of the bulk modulus along the [100] and [10] directions are significantly larger than those along the [1] direction. As shown in Table 5, the $B[100]/B[1]$ values of Ti_2lnC and Ti_2lnN are 1.08 and 1.90, respectively. The $B[100]/B[1]$ values of Zr_2lnC and Zr_2lnN are 1.03 and 1.04, respectively. It can be seen that Ti_2lnN has the largest anisotropy, which can be clearly perceived in combination with the 2D diagram, showing that the compression ratio along the *c*-axis is smaller than the *a*-axis and *b*-axis compression [39,40].

3.5. Debye Temperatures and Anisotropy of Sound Velocities

The Debye temperature (θ_D) is a fundamental thermodynamic property of a solid. The Debye temperature is commonly used to characterize a material's thermal properties, which may be computed using the single crystal elastic constant [41]:

$$\theta_D = \frac{h}{k_B}\left[\frac{3n}{4\pi}\left(\frac{N_A\rho}{Mc}\right)\right]^{\frac{1}{3}} v_m \tag{16}$$

N_A stands for Avogadro's constant, k_B is Boltzmann's constant, and h is Planck's constant. the total number of atoms in the unit cell is represented by n. M stands for molecular weight, ρ is density, and v_m represents the average sound velocity, which is determined by the longitudinal and transverse sound velocities, as shown in the following equation [42,43]:

$$v_l = \left[\left(B+\frac{4G}{3}\right)/\rho\right]^{\frac{1}{2}} \tag{17}$$

$$v_t = \left(\frac{G}{\rho}\right)^{\frac{1}{2}} \tag{18}$$

$$v_m = \left[\frac{1}{3}\left(\frac{2}{v_t^3}+\frac{1}{v_l^3}\right)\right]^{-\frac{1}{3}} \tag{19}$$

Table 6 shows the calculated values of v_l, v_t, v_m, and θ_D for the compounds. In general, the greater the density, the slower the sound speed. Due to the higher densities of Ti_2lnN and Zr_2lnN (6.389 g/cm^3 for Ti_2lnN and 7.302 g/cm^3 for Zr_2lnN), their sound velocities are relatively slow in Table 6.

Table 6. The density ρ, sound velocities (longitudinal v_l, transverse v_t, and mean v_m), and Debye temperature θ_D of M_2InX (M = Ti, Zr and X = C, N) MAX phases.

TM_5Al_3C	ρ (g/cm^3)	v_l(km/s)	v_t (km/s)	v_m(km/s)	θ_D (K)	Ref.
Ti_2lnC	6.079	6.738	4.271	4.697	564	This work
Ti_2lnN	6.389	6.013	3.555	3.938	480	This work
Zr_2lnC	6.949	6.066	3.573	3.960	446	This work
Zr_2lnN	7.302	5.791	3.362	3.731	426	This work
		5.770	3.297		423	Theo. [23]

Figure 9a shows the variation in different sound velocities. Ti_2lnC has the highest Debye temperature due to its low density and high elastic modulus, and Zr_2lnN has the lowest Debye temperature due to its high density and low elastic modulus. As we all know, the Debye temperature is commonly employed to reflect the strength of chemical bonds and the hardness of materials. As a result, the higher the Debye temperature, the stronger the chemical bond and the harder the solid.

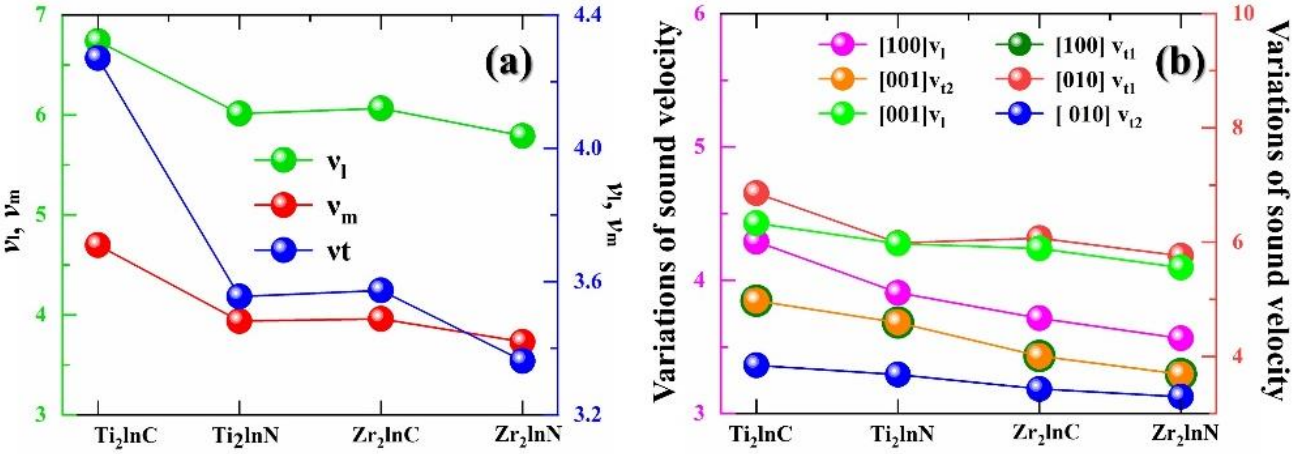

Figure 9. (**a**) Variations in sound velocity of M_2InX (M = Ti, Zr and X = C, N) MAX phases; (**b**) Directional sound velocity of M_2InX (M = Ti, Zr and X = C, N) MAX phases.

It can be shown that Ti_2lnC has the highest Debye temperature (564 K), suggesting that its chemical bond is the strongest, while Zr_2lnN has the lowest (426 K), showing that its chemical bond is the weakest. At the same time, it can be demonstrated that Ti_2lnC has the highest hardness and Zr_2lnN has the lowest. This confirms the previous section's conclusion about the materials' strength and hardness based on the elastic constant.

In addition, there is a certain proportional relationship between Debye temperature and thermal conductivity, so the higher the Debye temperature of the material, the greater the thermal conductivity, which is consistent with the literature [44–46]. Therefore, Ti_2lnC has the largest Debye temperature and thus exhibits the largest thermal conductivity.

The transverse sound velocity has two modes: v_{t1} (first transverse mode) and v_{t2} (second transverse mode). The directional sound velocity calculation results of M_2InX phases are shown in Table 7. Table 7 shows that the first transverse sound velocity ([10]v_{t1}) of the M_2InX system along the [100] direction is the greatest, followed by the first longitudinal sound velocity ([1]v_l). The directional sound velocity is well-known to be related to the elastic constants (C_{11}, C_{33}, C_{44}). As a result, Figure 9b shows the relationship between the elastic constants of sound velocity in different directions for the M_2InX phases. All sound speeds are obviously anisotropic in both Ti_2lnX (X = C, N) and Zr_2lnX (X = C, N) systems due to the shift in sound speed direction. It is also demonstrated that the link between sound speed and elastic constant is consistent. For example, the initial transverse sound velocity ([10]v_{t1}) along the [100] direction is related to C_{11}, for which the order is Ti_2lnC > Zr_2lnC > Ti_2lnN > Zr_2lnN. Similarly, the change trend of [1]v_1 matches that of C_{33}, and the change trend of [1]v_{t2}, [100]v_{t1}, and [10]v_{t2} matches that of C_{44}. [100]v_l is associated with C_{11}-C_{12}. Therefore, Figure 9b plots the relationship between different sound velocities for M_2InX phases.

Table 7. Anisotropic sound velocities (m/s) of M_2InX (M = Ti, Zr and X = C, N) MAX phases.

	[100]			[1]		
	[100]v_l	[10]v_{t1}	[1]v_{t2}	[1]v_l	[100]v_{t1}	[10]v_{t2}
Ti_2lnC	4289	6858	3846	6331	3846	3846
Ti_2lnN	3906	5985	3683	5974	3683	3683
Zr_2lnC	3715	6070	3431	5888	3431	3431
Zr_2lnN	3564	5760	3295	5555	3295	3295

3.6. Thermal Properties

Generally speaking, the thermal properties of materials are usually characterized by thermal conductivity, heat capacity, and thermal expansion coefficient. Thermal conductivity is a measure of the thermal conductivity of a substance. The lattice thermal conductivity

k_{ph} is one of the most important indicators to describe the thermal behavior of solids. Therefore, according to Slack's model [47], the lattice thermal conductivity of M_2InX phases can be calculated with the following empirical formula:

$$k_{ph} = A\frac{M_{av}\delta\theta_D^3}{\gamma^2 T n^{2/3}} \tag{20}$$

Here, the volume of each atom is denoted by δ^3. The average atomic mass of each atom is denoted by M_{av}, T is the temperature, and n is the number of atoms in the unit cell. γ is the Grüneisen parameter that can be obtained from Poisson's ratio v, while A_γ is the component associated with γ, and the formulas are as follows [48]:

$$\gamma = \frac{3(1+v)}{2(2-3v)} \tag{21}$$

$$A_\gamma = \frac{5.720 \times 10^7 \times 0.849}{2 \times \left(1 - \frac{0.154}{\gamma} + \frac{0.228}{\gamma^2}\right)} \tag{22}$$

The lattice thermal conductivities of Ti_2InC, Ti_2InN, Zr_2InC, and Zr_2InN at two temperatures (300 K and 1300 K) are shown in Table 8. The results show that most of the M_2AX phases have thermal conductivities ranging from 12 to 60 $W \cdot m^{-1}$ [49]. The calculation result is within this range. The lattice thermal conductivities of Ti_2InC, Ti_2InN, Zr_2InC, and Zr_2InN at room temperature (300 K) are 51.48, 20.43, 23.59, and 19.42 $W \cdot m^{-1} \cdot K^{-1}$, respectively. Therefore, Ti_2InC, Ti_2InN, Zr_2InC, and Zr_2InN can serve as potential thermal conductive materials at room temperature. As shown in Figure 10, as the temperature increases, k_{ph} decreases rapidly and then tends to a limit value. In the temperature range of 300 K–1300 K, the order of k_{ph} is $Ti_2InC > Zr_2InC > Ti_2InN > Zr_2InN$.

Table 8. Calculated δ (in Å), M_{av} (in kg/mol), Grüneisen parameter γ, A_γ ($\times 10^{-8}$), and lattice thermal conductivities k_{ph} (in $W \cdot m^{-1} \cdot K^{-1}$) of M_2InX (M = Ti, Zr and X = C, N) MAX phases.

	δ	M_{av}	γ	n	A_γ	k_{ph} (300 K)	k_{ph} (1300 K)	k_{min}
Ti_2InC	2.48	55.66	1.16	8.00	3.34	51.48	11.88	1.23
Ti_2InN	2.44	56.16	1.41	8.00	3.24	20.43	4.72	1.12
Zr_2InC	2.60	77.31	1.43	8.00	3.23	23.59	5.44	0.96
Zr_2InN	2.64	77.81	1.48	8.00	3.21	19.42	4.48	0.94

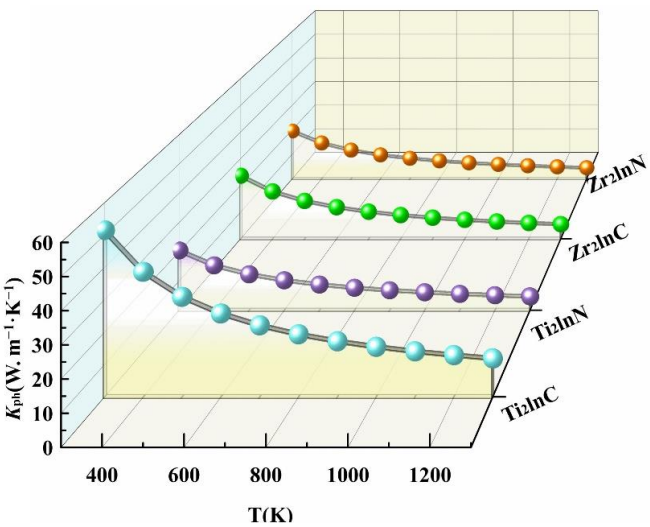

Figure 10. Lattice thermal conductivities k_{ph} of M_2InX (M = Ti, Zr and X = C, N) MAX phases in the temperature range of 300 K–2000 K.

The thermal conductivity is mainly derived from the lattice thermal conductivity at the ground state temperature. Therefore, the thermal conductivity reflection of ceramics can be characterized as the minimum thermal conductivity [50]. Consequently, the Clark model is used here to calculate the minimum thermal conductivity $k_{\min}$ of the M_2InX system, and the expression is as follows:

$$k_{min} = K_B V_m \left(\frac{n\rho N_A}{M} \right)^{\frac{2}{3}} \tag{23}$$

Table 8 shows the calculated minimum lattice thermal conductivities for the M_2InX system. It can be seen from Table 8 that the $k_{\min}$ of M_2InX are 1.23, 1.12, 0.96, and 0.94 $W \cdot m^{-1} \cdot K^{-1}$, respectively. The difference between the lattice thermal conductivity and θ_D is that the higher Debye temperature has a larger lattice thermal conductivity, so Ti_2lnC has the largest thermal conductivity, which corresponds to the highest Debye temperature (564 K) of Ti_2lnC. Furthermore, the calculated order of minimum thermal conductivity is $Ti_2lnC > Ti_2lnN > Zr_2lnC > Zr_2lnN$. As is known, M_2InX phases are not potential high-temperature thermal barrier coatings when compared with $Ln_2Zr_2O_7$ (1.2~1.4 $W \cdot m^{-1} \cdot K^{-1}$) [51]. The thermal conductivity of new ceramic materials is between 1.2 $W \cdot m^{-1} \cdot K^{-1}$–1.6 $W \cdot m^{-1} \cdot K^{-1}$. Among these compounds, the thermal conductivity of Ti_2lnC is within this range, so Ti_2lnC may become a potential insulating material [52].

3.7. Electronic Properties

The electronic properties (density of states) of M_2InX (M = Ti, Zr and X = C, N) MAX phases were studied to better understand chemical bonding and bond behaviors. Figure 11 depicts the M_2InX phases' total density of states (TDOS) and partial density of states (PDOS). To begin, it is clear that DOS has a significant finite value at the Fermi level, indicating that these compounds exhibit metallic conductivity. Figure 11 shows that the total density of states (E_f) value of Ti_2InN and Zr_2lnN is greater than that of Ti_2InC and Zr_2lnC, indicating that Ti_2InN and Zr_2lnN are more conductive than Ti_2InC and Zr_2lnC. Secondly, the peak topologies and relative heights of the peaks around E_f in the TDOS plot are highly comparable, indicating the presence of similar chemical bonds in Zr_2AN. The time difference around the Fermi level is mostly made up of ln-*p* and M-*d* states. The time difference below the Fermi energy is caused mostly by the X-*s*, M-*s*, and M-*p* states, whereas the time difference above the Fermi energy is caused primarily by the ln-*s* and X-*p* states. As shown in Figure 11, the ln-*p*, M-*d*, and X-*p* states exhibit substantial hybridization, allowing M-C and M-N chemical bonds to form, resulting in the high elastic modulus of M_2InX. PDOS exhibits multiple hybridizations of the electronic states M, ln, and X. The valence band of M_2InX in Figure 11 displays substantial hybridization of the M-*d* and X-*p* states, as predicted for covalent compounds. The *d*-*p* hybrid state corresponding to the M-ln bond was discovered to be in a greater energy range than the M-X bond. As a result, the M-X *d*-*p* hybridization helps to maintain the crystal structure. Finally, it is demonstrated that M's electronic charge density almost overlaps that of ln, indicating that the bonding between M and ln is quite weak. These findings are consistent with the observation that the biggest phase features very strong M-X bonds and very weak M-ln bonds.

As can be seen from Table 9, the M atom loses electrons, while the ln and X atoms gain electrons. Among them, for the Ti_2InX system, the Ti-C bond has the largest BP value, indicating that the Ti-C bond has a strong chemical bond. Therefore, it is proved that Ti_2lnC has the strongest chemical bond and Ti_2lnN has the weakest chemical bond. For the Zr_2InX system, it can also be stated that Zr_2InC has the strongest chemical bond and Zr_2InN has the weakest chemical bond. The M and X atoms form a strongly directed M-X covalent bond originating from the hybrid M *d*-X *p* state. These results are also consistent with the finding that the largest phase typically has very strong M-X bonds and relatively weak M-A bonds.

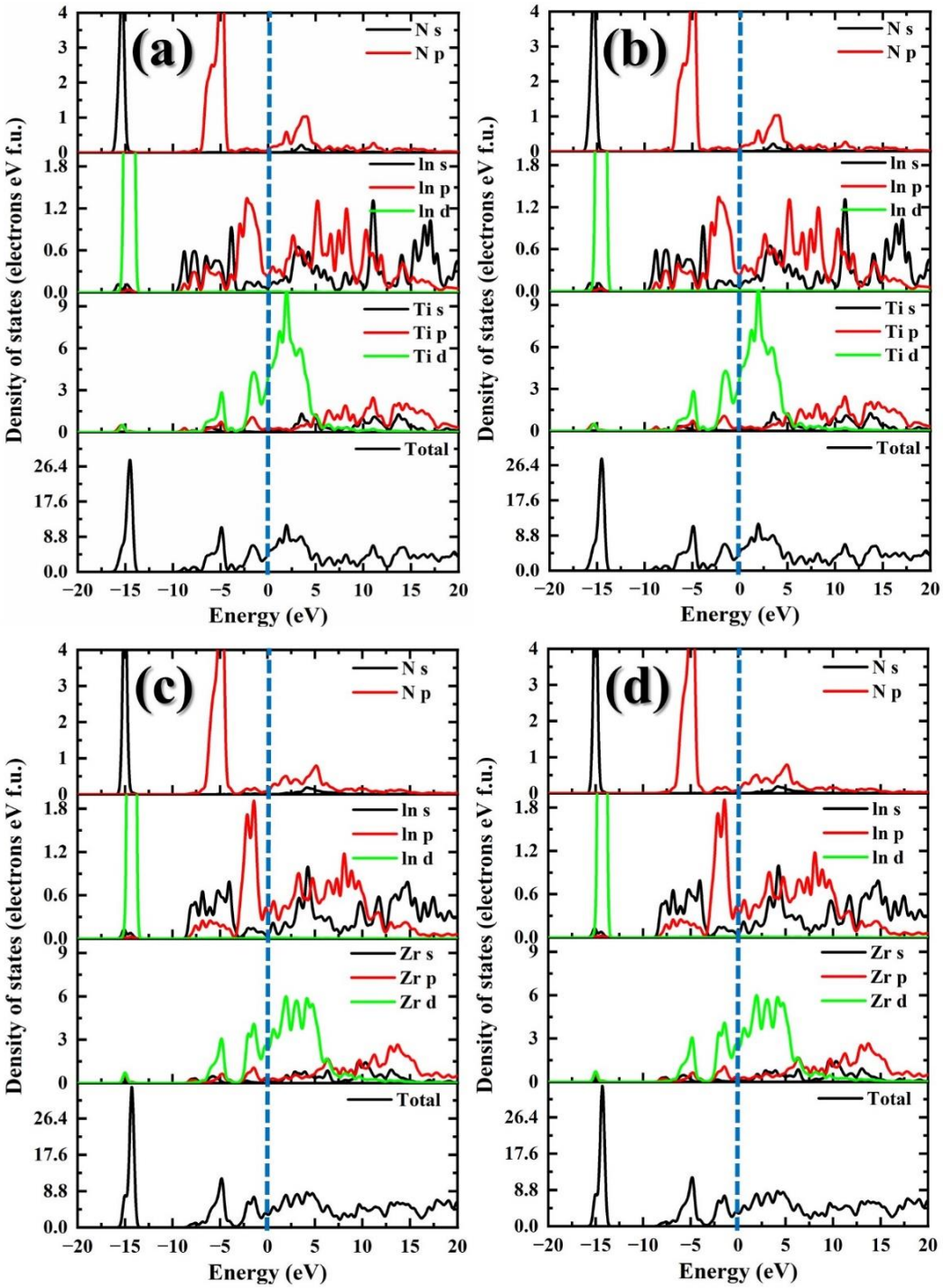

Figure 11. The calculated total and partial density of states for (**a**) Ti_2InC, (**b**) Ti_2InN, (**c**) Zr_2InC, and (**d**) Zr_2InN.

Table 9. Calculated Mulliken charge and bond population (BP) analysis of M_2InX (M = Ti, Zr and X = C, N) MAX phases.

	Atom	Charge Number					Charge	Bond	BP	Length(Å)
		s	*p*	*d*	*f*	Total				
Ti_2InC	Ti	2.18	6.79	2.66	0.00	11.62	0.38	Ti-C	1.04	2.12
	In	1.11	1.94	9.97	0.00	13.02	−0.02			
	C	1.46	3.27	0.00	0.00	4.73	−0.73			
Ti_2InN	Ti	2.19	6.77	2.69	0.00	11.65	0.35	Ti-N	0.76	2.10
	In	1.05	1.97	9.97	0.00	12.99	0.01			
	N	1.68	4.04	0.00	0.00	5.71	−0.71			
Zr_2InC	Zr	2.28	6.63	2.68	0.00	11.59	0.41	Zr-C	1.06	2.30
	In	1.11	1.93	9.98	0.00	13.02	−0.02			
	C	1.49	3.31	0.00	0.00	4.80	−0.80			
Zr_2InN	Zr	2.30	6.63	2.72	0.00	11.65	0.35	Zr-N	0.69	2.27
	In	1.03	1.92	9.97	0.00	12.92	0.08			
	N	1.70	4.07	0.00	0.00	5.77	−0.77			

4. Conclusions

In summary, this work uses first-principles calculations to estimate the anisotropic elastic and thermal properties of M_2InX (M = Ti, Zr and X = C, N) MAX phases. The structural properties and elastic constants of the obtained M_2InX phases are in agreement with the results reported in the literature, the obtained data are quite reliable, and the M_2InX phase's mechanical stability has been studied. According to the elastic constants, Ti_2InC and Zr_2InC are more incompressible along the *a*- and *b*-axes, while Ti_2InN and Zr_2InN are more compressible along the *a*- and *b*-axes. For all M_2InX phase materials, shear modulus is a better measure of hardness than bulk modulus. Therefore, Ti_2InC has high hardness and can be used to make superhard materials. The anisotropic elasticity of the M_2InX phase is $Ti_2InN > Ti_2InC$, $Zr_2InN > Zr_2InC$, based on A^U, A_{comp}, and A_{shear} values, 3D graphs, and 2D projection analysis. In addition, Ti_2InC has the highest speed of sound (4.697) and Debye temperature (564 K), while Zr_2InN has the lowest speed of sound (3.731) and Debye temperature (426 K). Meanwhile, Ti_2InC may become a potential insulation material. The electronic properties of the M_2InX phase were investigated, and the presence of strong M-X *d*-*p* hybridization helps to maintain the crystal structure.

Author Contributions: Conceptualization, writing—review and editing, supervision, funding acquisition, Y.D.; data curation, M.P.; writing—original draft preparation, B.L.; visualization, L.S.; formal analysis, H.Q. All authors have read and agreed to the published version of the manuscript.

Funding: This research received no external funding or This research was funded by the Rare and Precious Metal Materials Genome Engineering Project of Yunnan Province (Y.D.: 202002AB080001), Yunnan Ten Thousand Talents Plan Young and Elite Talents Project (Y.D.: YNWR-QNBJ-2018-044) and the National Natural Science Foundation of China (M.P.: 51761023).

Institutional Review Board Statement: Not applicable.

Informed Consent Statement: Not applicable.

Data Availability Statement: Not applicable.

Conflicts of Interest: The authors declare no conflict of interest.

References

1. Qian, X.K.; He, X.D.; Li, Y.B. Cyclic oxidation of Ti_3AlC_2 at 1000–1300 °C in air. *Corros. Sci.* **2011**, *53*, 290–295. [CrossRef]
2. Lin, Z.J.; Li, M.S.; Wang, J.Y.; Zhou, Y.C. High-temperature oxidation and hot corrosion of Cr_2AlC. *Acta Mater.* **2007**, *55*, 6182–6191. [CrossRef]
3. Zhou, A.G.; Barsoum, M.W. Kinking nonlinear elastic deformation of Ti_3AlC_2, Ti_2AlC, Ti_3Al $(C_{0.5}, N_{0.5})_2$ and Ti_2Al $(C_{0.5}, N_{0.5})$. *J. Alloys Compd.* **2010**, *498*, 62–70. [CrossRef]

4. Qian, X.; He, X.; Li, Y.; Sun, Y.; Zhu, C. Improving the Cyclic-Oxidation Resistance of Ti_3AlC_2 at 550 °C and 650 °C by Preoxidation at 1100 °C. *Int. J. Appl. Ceram. Tec.* **2010**, *6*, 760–765. [CrossRef]
5. Eriksson, A.O.; Zhu, J.Q.; Ghafoor, N.; Jensen, J.; Greczynski, G.; Johansson, M.P.; Rosén, J. Ti–Si–C–N thin films grown by reactive arc evaporation from Ti_3SiC_2 cathodes. *J. Mater. Res.* **2011**, *26*, 874–881. [CrossRef]
6. Zhu, H.P.; Qian, X.K.; Wu, H.Y.; Lei, J.; Song, Y.; He, X.; Zhou, Y. Cyclic Oxidation of Ternary Layered Ti_2AlC at 600–1000 °C in Air. *Int. J. Appl. Ceram. Tec. L.* **2015**, *12*, 403–410. [CrossRef]
7. Barsoum, M.W. The $M_{N+1}AX_N$ phases: A new class of solids: Thermodynamically stable nanolaminates. *Prog. Solid. State. Ch.* **2000**, *28*, 201–281. [CrossRef]
8. Eklund, P.; Beckers, M.; Jansson, U.; Högberg, H.; Hultman, L. The $M_{n+1}AX_n$ phases: Materials science and thin-film processing. *Thin Solid Films* **2010**, *518*, 1851–1878. [CrossRef]
9. Qian, X.; Li, Y.; Sun, Y.; He, X.; Zhu, C. Cyclic oxidation behavior of TiC/Ti_3AlC_2 composites at 550–950 °C in air. *J. Alloys Compd.* **2010**, *491*, 386–390. [CrossRef]
10. Whittle, K.R.; Blackford, M.G.; Aughterson, R.D.; Moricca, S.; Lumpkin, G.R.; Riley, D.P.; Zaluzec, N.J. Radiation tolerance of Mn+1AXn phases, Ti_3AlC_2 and Ti_3SiC_2. *Acta Mater.* **2010**, *58*, 4362. [CrossRef]
11. Utili, M.; Agostini, M.; Coccoluto, G.; Lorenzini, E. Ti_3SiC_2 as a candidate material for lead cooled fast reactor. *Nucl. Eng. Des.* **2011**, *241*, 1295–1300. [CrossRef]
12. Yang, Z.J.; Tang, L.; Guo, A.M.; Cheng, X.L.; Zhu, Z.H.; Yang, X.D. Origin of c-axis ultraincompressibility of Zr_2InC above 70 GPa via first-principles. *J. Appl. Phys.* **2013**, *114*, 083506. [CrossRef]
13. Bortolozo, A.D.; Serrano, G.; Serquis, A.; Rodrigues, D., Jr.; Santos, C.A.M.D.; Fisk, Z.; Machado, A.J.S. Superconductivity at 7.3 K in Ti_2InN. *Solid State Commun.* **2010**, *150*, 1364–1366. [CrossRef]
14. Sun, Z.M.; Music, D.; Ahuja, R.; Schneider, J.M. Theoretical investigation of the bonding and elastic properties of nanolayered ternary nitrides, Schneider. *Phys. Rev. B* **2005**, *71*, 193402. [CrossRef]
15. Bao, L.; Qu, D.; Kong, Z.; Duan, Y. Predictions of structural, electronic, mechanical, and thermodynamic properties of TMBCs (TM= Ti, Zr, and Hf) ceramics. *J. Am. Ceram. Soc.* **2020**, *103*, 5232–5247. [CrossRef]
16. Kohn, W.; Sham, L.J. Self-consistent equations including exchange and correlation effects. *Phys. Rev.* **1965**, *140*, 1133–1138. [CrossRef]
17. Segall, M.D.; Lindan, P.J.D.; Probert, M.J.; Pichard, C.J.; Hasnip, P.J.; Clark, S.J.; Payne, M.C. First-principles simulation: Ideas, illustrations and the CASTEP code. *J. Phys. Condens. Mater.* **2002**, *14*, 2717–2744. [CrossRef]
18. Pacheco-Kato, J.C.; del Campo, J.M.; Gázquez, J.L.; Trickey, S.B.; Vela, A. A PW91-like exchange with a simple analytical form. *Chem. Phys. Lett.* **2016**, *651*, 268–273. [CrossRef]
19. Monkhorst, H.J.; Pack, J.D. Special points for Brillouin-zone integrations. *Phys. Rev. B* **1976**, *13*, 5188. [CrossRef]
20. Vanderbilt, D. Soft self-consistent pseudopotentials in a generalized eigenvalue formalism. *Phys. Rev. B* **1990**, *41*, 7892. [CrossRef]
21. Perdew, J.P.; Chevary, J.A.; Vosko, S.H.; Jackson, K.A.; Pederson, M.R.; Singh, D.J.; Fiolhais, C. Erratum: Atoms, molecules, solids, and surfaces: Applications of the generalized gradient approximation for exchange and correlation. *Phys. Rev. B* **1992**, *46*, 6671. [CrossRef] [PubMed]
22. Barsoum, M.W.; Golczewski, J.; Seifert, H.J. Fabrication and electrical and thermal properties of Ti_2InC, Hf_2InC and $(Ti, Hf)_2InC$. *J. Alloys Compd.* **2002**, *340*, 173–179. [CrossRef]
23. Wu, H.; Qian, X.; Zhu, H. First-principles study of the structural, electronic and elastic properties of ternary Zr_2AN (A = Ga, In and Tl). *Comp. Mater. Sci.* **2014**, *84*, 103–107. [CrossRef]
24. Horlait, D.; Middleburgh, S.; Chroneos, A.; Lee, W.E. Synthesis and DFT investigation of new bismuth-containing MAX phases. *Sci. Rep.* **2016**, *6*, 18829. [CrossRef]
25. Wang, X.; Bao, L.; Wang, Y.; Wu, Y.; Duan, Y.; Peng, M. Explorations of electronic, elastic and thermal properties of tetragonal TM_4N_3 (TM= V, Nb and Ta) nitrides. *Mater. Today Commun.* **2021**, *26*, 101723. [CrossRef]
26. Karki, B.B.; Ackland, G.; Crian, J. Elastic instabilities in crystals from ab initio stress- strain relations. *J. Phys. Condens. Matter* **1997**, *9*, 8579–8589. [CrossRef]
27. Shou, H.; Duan, Y. Anisotropic elasticity and thermal conductivities of (α, β, γ)-$LiAlSi_2O_6$ from the first-principles calculation. *J. Alloys Compd.* **2018**, *756*, 40–49. [CrossRef]
28. Zhang, X.H.; Luo, X.G.; Han, J.C.; Li, J.P.; Han, W.B. Electronic structure, elasticity and hardness of diborides of zirconium and hafnium: First principles calculations. *Comput. Mater. Sci.* **2008**, *4*, 411–421. [CrossRef]
29. Khazaei, M.; Arai, M.; Sasaki, T.; Estili, M.; Sakka, Y. Trends in electronic structures and structural properties of MAX phases: A first-principles study on M_2AlC (M = Sc, Ti, Cr, Zr, Nb, Mo, Hf, or Ta), M_2AlN, and hypothetical M_2AlB phases. *J. Phys. Condeens. Mat.* **2014**, *26*, 505503. [CrossRef]
30. Lapauw, T.; Lambrinou, K.; Cabioc'h, T.; Halim, J.; Lu, J.; Pesach, A.; Rivin, O.; Ozeri, O.; Caspi, E.N.; Hultman, L.; et al. Synthesis of the new MAX phase Zr_2AlC. *J. Eur. Ceram. Soc.* **2016**, *36*, 1847–1853. [CrossRef]
31. Medkour, Y.; Bouhemadou, A.; Roumili, A. Structural and electronic properties of M_2InC (M = Ti, Zr, and Hf). *Solid State Commun.* **2008**, *148*, 459–463. [CrossRef]
32. Ranganathan, S.I.; Ostoja-Starzewski, M. Universal elastic anisotropy index. *Phys. Rev. Lett.* **2008**, *101*, 055504. [CrossRef]
33. Thomsen, L. Weak elastic anisotropy. *Geophysics* **1986**, *51*, 1954–1966. [CrossRef]

34. Ravindran, P.; Fast, L.; Korzhavyi, P.A.; Johansson, B. Density functional theory for calculation of elastic properties of orthorhombic crystals: Application to $TiSi_2$. *J. Appl. Phys.* **1998**, *84*, 4891–4904. [CrossRef]
35. Ledbetter, M.H. Elastic properties of zinc: A compilation and a review. *J. Phys. Chem. Ref. Data* **1977**, *6*, 1181–1203. [CrossRef]
36. Nye, J.F. Physical properties of crystals. *Mater. Today* **2007**, *10*, 53.
37. Hearmon, R.F.S.; Maradudin, A.A. An introduction to applied anisotropic elasticity. *Phys. Today* **1961**, *14*, 48. [CrossRef]
38. Li, B.; Duan, Y.; Peng, M. Theoretical insights on elastic anisotropy and thermal anisotropy of TM_5Al_3C (TM= Zr, Hf, and Ta) carbides. *Vacuum* **2022**, *200*, 110989. [CrossRef]
39. Peng, M.; Wang, R.; Wu, Y. Elastic anisotropies, thermal conductivities and tensile properties of MAX phases Zr_2AlC and Zr_2AlN: A first-principles calculation. *Vacuum* **2022**, *196*, 110715. [CrossRef]
40. Bao, W.; Liu, D.; Duan, Y. A first-principles prediction of anisotropic elasticity and thermal properties of potential superhard WB_3. *Ceram. Int.* **2018**, *44*, 14053–14062. [CrossRef]
41. Anderson, O.L. A simplified method for calculating the Debye temperature from elastic constants. *J. Phys. Chem. Solid.* **1963**, *2490*, 9–17. [CrossRef]
42. Arab, F.; Sahraoui, F.A.; Haddadi, K.; Bouhemadou, A.; Louail, L. Phase stability, mechanical and thermodynamic properties of orthorhombic and trigonal $MgSiN_2$: An ab initio study. *Phase Transit.* **2016**, *89*, 480–513. [CrossRef]
43. Chen, S.; Sun, Y.; Duan, Y.H.; Huang, B.; Peng, M.J. Phase stability, structural and elastic properties of C15-type Laves transition-metal compounds MCo2 from first-principles calculations. *J. Alloys Compd.* **2015**, *630*, 202–208. [CrossRef]
44. Benayad, N.; Rached, D.; Khenata, R. First principles study of the structural, elastic and electronic properties of Ti_2InC and Ti_2InN. *Mod. Phys. Lett. B* **2011**, *25*, 747–761. [CrossRef]
45. Yang, Z.J.; Li, J.; Linghu, R.F.; Cheng, X.L.; Yang, X.D. First-principle investigations on the structural dynamics of Ti_2GaN. *J. Alloys Compd.* **2013**, *574*, 573–579. [CrossRef]
46. He, X.; Bai, Y.; Li, Y.; Zhu, C.; Li, M. Ab initio calculations for properties of MAX phases Ti_2InC, Zr_2InC, and Hf_2InC. *Solid State Commun.* **2009**, *149*, 564–566. [CrossRef]
47. Morelli, D.T.; Slack, G.A.; Shinde, S.L.; Goela, J.S. (Eds.) *High Thermal Conductivity Materials*; Springer: New York, NY, USA, 2006.
48. Julian, C.L. Theory of heat conduction in rare-gas crystals. *Phys. Rev.* **1965**, *137*, A128. [CrossRef]
49. Barsoum, M.W. *MAX Phases: Properties of Machinable Ternary Carbides and Nitrides*; John Wiley & Sons: Weinheim, Germany, 2013.
50. Li, S.; Sun, W.; Luo, Y. Pushing the limit of thermal conductivity of MAX borides and MABs. *J. Mater. Sci. Technol.* **2021**, *97*, 87–106. [CrossRef]
51. Feng, J.; Xiao, B.; Wan, C.L.; Qu, Z.X.; Huang, Z.C.; Chen, J.C.; Zhou, R.; Pan, W. Electronic structure, mechanical properties and thermal conductivity of $Ln_2Zr_2O_7$ (ln = La, Pr, Nd, Sm, Eu and Gd) pyrochlore. *Acta Mater.* **2011**, *59*, 1742–1760. [CrossRef]
52. Yang, A.; Bao, L.; Peng, M.; Duan, Y. Explorations of elastic anisotropies and thermal properties of the hexagonal $TMSi_2$ (TM = Cr, Mo, W) silicides from first-principles calculations. *Mater. Today Commun.* **2021**, *27*, 102474. [CrossRef]